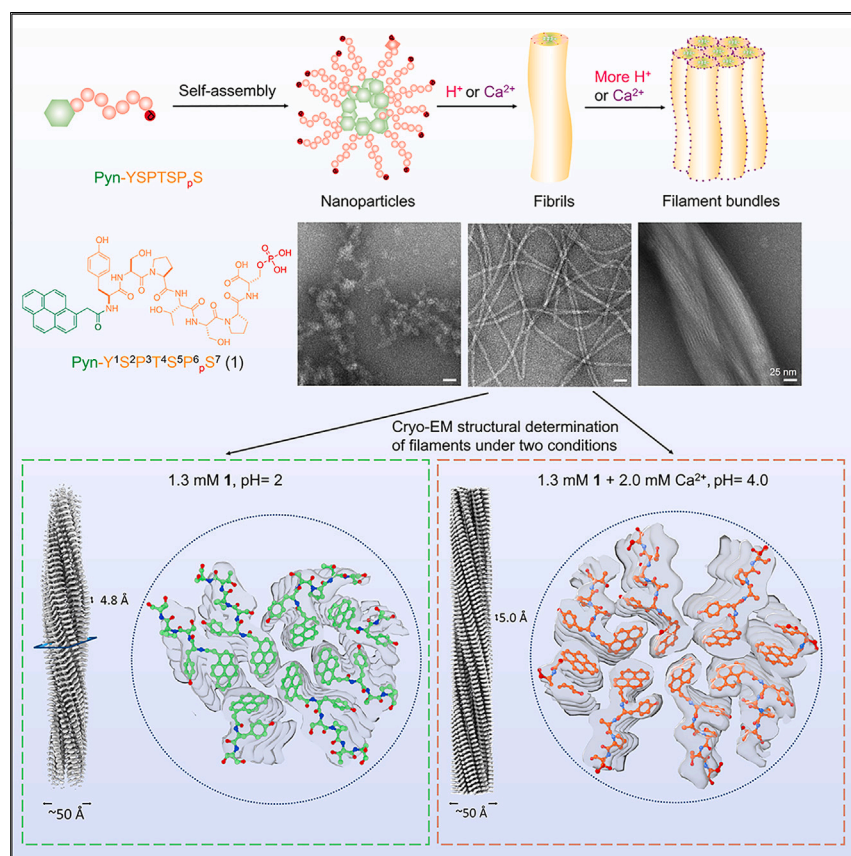


Article

Hierarchical assembly of intrinsically disordered short peptides



Cryo-EM reveals that aromatic packing from pyrenes enables the assemblies of intrinsically disordered peptides (IDPs), and subsequently, molecular engineering indicates that interfibrillar interactions create hierarchical assemblies. As the first example of atomistic structures of IDP assemblies, this work provides new insights to design the assemblies of IDPs and to understand the disorder-to-order transition in small molecule self-assembly in water.

Jiaqi Guo, Shane T. Rich-New, Chen Liu, ..., Edward H. Egelman, Fengbin Wang, Bing Xu

egelman@virginia.edu (E.H.E.)
jerrywang@uab.edu (F.W.)
bxu@brandeis.edu (B.X.)

Highlights

Hydrophobic interactions drive IDPs to self-assemble to form assemblies

Cryo-EM reveals the atomic structures of fibrillar assemblies of IDPs

Calcium ion switches the symmetry of IDP filaments from C1 to C2

Interfibrillar interactions confer filament bundles as higher-order assemblies

Article

Hierarchical assembly of intrinsically disordered short peptides

Jiaqi Guo,¹ Shane T. Rich-New,² Chen Liu,³ Yimeng Huang,¹ Weiyi Tan,¹ Hongjian He,¹ Meihui Yi,¹ Xixiang Zhang,³ Edward H. Egelman,^{4,*} Fengbin Wang,^{2,4,5,*} and Bing Xu^{1,6,*}

SUMMARY

The understanding of how short peptide assemblies transit from disorder to order remains limited due to the lack of atomistic structures. Here, we report the cryo-EM structure of the nanofibers short intrinsically disordered peptides (IDPs). On lowering pH or adding calcium ions, the IDP transitions from individual nanoparticles to nanofibers containing an aromatic core and a disordered periphery were composed of 2–5 amino acids. Protonating the phosphate or adding more metal ions further assembles the nanofibers into filament bundles. The assemblies of the IDP analogs with controlled chemistry, such as phosphorylation site, hydrophobic interactions, and sequences, indicate that metal ions interact with the flexible periphery of the nanoparticles of the IDPs to form fibrils and enhance the interfibrillar interactions to form filament bundles. Illustrating that an IDP self-assembles from disorder to order, this work offers atomistic molecular insights to understand assemblies of short peptides driven by noncovalent interactions.

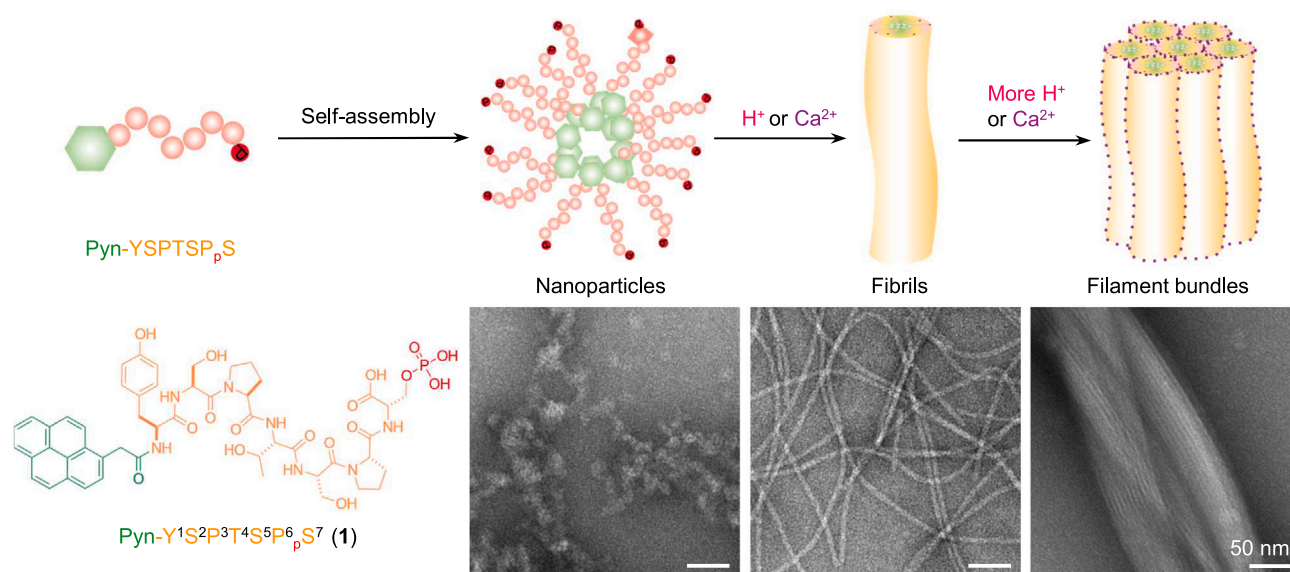
INTRODUCTION

This article reports the self-assembly of an intrinsically disordered peptide (IDP). IDPs are the peptide sequences from intrinsically disordered regions (IDRs) of proteins.¹ Despite intensive exploration of the peptide assemblies that adopt well-defined conformations, such as α helices^{2,3} and β sheet,^{4–10} for various applications,^{11–22} the self-assembly of IDPs is much less explored.^{23–26} Particularly, there are very limited numbers of structures of IDP assemblies (i.e., the disorder is still preserved in the nanofibers) except human amyloid fibers, such as Ab42²⁷ recently determined by cryoelectron microscopy (cryo-EM). It would be of great interest if we can understand the main driving forces for the self-assembly of IDPs, including the modulatory effect of posttranslational modification (PTM) on self-assembly, the effect of metal ions on enabling self-assembly, and most importantly, the atomistic structures of IDP assemblies.

To partially address the above important questions, we conjugated an aromatic motif and introduced a phosphate group to a heptapeptide, YSPTSPS (Y = tyrosine, S = serine, P = proline, and T = threonine) that is derived from a validated IDR,²⁸ via solid-phase peptide synthesis (Scheme S1) to generate an IDP (1) for interacting with metal ions. The phosphopeptide (1) contains pyrene as the aromatic motif, Y¹S²P³T⁴S⁵P⁶S⁷ as the IDP, and phosphorylation at the C-terminal serine (S7) as a representative PTM (Scheme 1). Using fluorescence spectroscopy and negative-stained EM, we found that 1 self-assembles to form nanofibers. With cryo-EM,²⁹ we determined the structure of the nanofibers of 1 in the presence or absence of Ca²⁺ at a resolution of 3.0 and 3.1 Å, respectively, judged by the “gold-standard”

THE BIGGER PICTURE

Small molecules self-assemble to form higher-order nanostructures that act as functional materials. However, *a priori* design of small molecules for self-assembly remains a grand challenge due to the limited understanding of the transition from disorder to order and the lack of structures of such assemblies. The guaranteed disorder phase of IDPs makes them the ideal targets for studying disorder-to-order transition in supramolecular assemblies. This work reveals the atomistic structures of the IDP assemblies, a poorly characterized and the most disordered subgroup of peptides, and uses molecular engineering to identify several key factors that contribute to the disorder-to-order transition. Elucidating the driving force, stimuli response, and structures of short IDP assemblies will not only establish IDP sequences as a new molecular platform to build hierarchical superstructures but may also offer useful insights to antagonize pathological IDPs, such as beta-amyloids.



Scheme 1. Illustration of the hierarchical assembly of an IDP and the corresponding assemblies at three stages

Fourier shell correlation (FSC) method. Interestingly, under both conditions, only one type of filamentous morphology is observed, but the helical symmetry of the two conditions is different. In both fiber structures, a conserved packing pattern was observed: the aromatic groups and N-terminal residues constitute the core of the nanofiber; certain disordered C-terminal residues and the phosphate group at the C terminus form the flexible periphery. Different design strategies that may attribute to nanofiber formation, such as alteration of the phosphorylation site, hydrophobic motif, and amino acid composition, were also examined. Using fluorescence spectroscopy, negative-stain EM, circular dichroism (CD), high-angle annular dark-field scanning transmission EM (HAADF-STEM), and energy-dispersive X-ray spectroscopy (EDS), we further demonstrate that divalent metal ions mediate the transition of nanofibers to filament bundles (Scheme 1). Combining cryo-EM structural elucidation and molecular engineering, this study probes the hierarchical self-assembly of a short IDP and provides atomistic details on how order arises from intrinsically disordered small molecule building blocks. Such molecular insights may find applications in designing self-assembly materials and improve our understanding of the aggregation of pathogenic IDPs or proteins that are associated with neurodegenerative diseases.

RESULTS

Molecular design of the short IDP

We decided to study the self-assembly of **1** (Scheme 1) for several reasons. (1) YSPTSPS is an IDP from a validated IDR²⁸ and the C-terminal domain (CTD) of protein POLR2A.³⁰ (2) Although the prominent characteristic of IDRs is their low content of bulky hydrophobic amino acids, the functions of IDRs rely more on hydrophobic interactions than on polar-polar interactions.³¹ In addition, a recent study reported that attaching hydrophobic alkyl chains to an IDP results in the self-assembly of the IDP to form micelles.²⁴ Thus, we hypothesized that aromatic motifs would provide unique hydrophobic interactions to enhance the interactions among IDPs to promote the self-assembly of IDPs for generating nanoscale assemblies. (3) Compared with alkyl chains used for hydrophobic interactions in the recent report of peptide amphiphiles containing an IDP,²⁴ aromatic-aromatic interactions possess several

¹Department of Chemistry, Brandeis University, 415 South Street, Waltham, MA 02453, USA

²Department of Biochemistry and Molecular Genetics, University of Alabama at Birmingham, Birmingham, AL 35233, USA

³Physical Science and Engineering Division, King Abdullah University of Science and Technology, Thuwal 23955-6900, Saudi Arabia

⁴Department of Biochemistry and Molecular Genetics, University of Virginia, Charlottesville, VA 22908, USA

⁵O'Neal Comprehensive Cancer Center, University of Alabama at Birmingham, Birmingham, AL 35233, USA

⁶Lead contact

*Correspondence: egelman@virginia.edu (E.H.E.), jerrywang@uab.edu (F.W.), bxu@brandeis.edu (B.X.)

<https://doi.org/10.1016/j.chempr.2023.04.023>

unique features: being well-established as a stabilizing force for proteins,³² aromatic-aromatic interactions should be a powerful strategy to control the self-assembly of IDPs; an aromatic motif, having a relatively compact volume compared with the bulky and long alkyl chains, would reduce the steric repulsion and conformational dynamics that are often associated with alkyl chains; usually adopting plane-to-plane or edge-to-plane orientation,³² aromatic-aromatic interactions result in more predictable and efficient molecular self-assembly. (4) As a local chemical change affecting proteins following the synthesis of proteins via the translation of mRNA, PTMs induce changes to protein structures, regulate protein function, and increase proteomic complexity. IDRs house large numbers of PTM sites in eukaryotic proteins,³³ which regulate their functions and structures.³⁴ Among various PTMs, we chose phosphorylation as a PTM of YSPTSPS because it strongly correlates with IDRs³⁵ and two-thirds of human proteins involve phosphorylation.³⁶ (5) Because metal ions can affect the aggregation of proteins containing IDRs,^{37,38} we also examined the response of the IDP assemblies to metal ions.

Cryo-EM reveals the self-assembly of short IDP

A precise structural description of the helical assemblies of IDPs remains a challenge in X-ray crystallography due to peptide packing incompatible with crystallographic space groups and solid-state NMR due to its limitation in determining long-range structure. The recent advances in cryo-EM have provided a unique opportunity to determine the structures of peptide assemblies,²⁹ including the assemblies of amyloid-like fibrils.^{27,39–41} Thus, we chose cryo-EM to determine the structures of the nanofibers formed by the self-assembly of 1. We collected the cryo-EM images of 1 at pH = 2 and at pH = 4 with 2.0 mM Ca²⁺ (Figures 1A and 1F). Under both conditions, only one species of nanofiber was observed from the reference-free 2D classification (Figures 1B, 1G, and S1A). The nanofiber's helical symmetry was determined by trial and error to test all possible symmetries indexed from the average power spectrum (Figures 1C and 1H) until recognizable peptide-like features were seen. At pH = 2, the nanofiber of 1 demonstrated C1 symmetry with a helical rise of 4.74 Å and a twist of 5.38°. At pH = 4 and 2.0 mM Ca²⁺, the nanofiber exhibited C2 point group symmetry with 4.95 Å helical rise and –3.80° helical twist. The resolution of each structure was estimated by map:map FSC (Figures S1B and S1C). The atomic model built into the 3D reconstruction shows parallel cross-β packing of 1, with seven or eight hydrophobic pyrene motifs residing in the center of the nanofiber, whereas the hydrophilic phosphoserines remain conformationally disordered on the outer surface of the nanofibers, where little density is observed in the cryo-EM map (Figures 1D, 1E, 1I, and 1J). This suggests that amino acids/residues not involved in helical packing remain conformationally flexible, resulting in a loss of Coulomb potential density in the maps, making model building impossible. Considering common conformers observed in other β sheet forming, amyloid-like filaments,⁴² it is quite unusual that this heptapeptide 1 self-assembles into only one type of cross-β filament. This phenomenon, we speculate, likely originates from that pyrene dominates the helical packing and provides extra restraints of inter-peptide interactions other than the typical hydrogen bonds formed between β sheets. In some other polymorphic amyloid filaments, on the other hand, the major interactions holding the filaments together are those β sheet hydrogen bonds. Those bonds are insensitive to a few degrees' change in the helical twist and therefore have some plasticity; hence, filaments will end up with a very flexible twist that leads to polymorphism.

Although the nanofibers display a uniform morphology under both conditions judged by 2D averages, it is unexpected that they possess a different helical

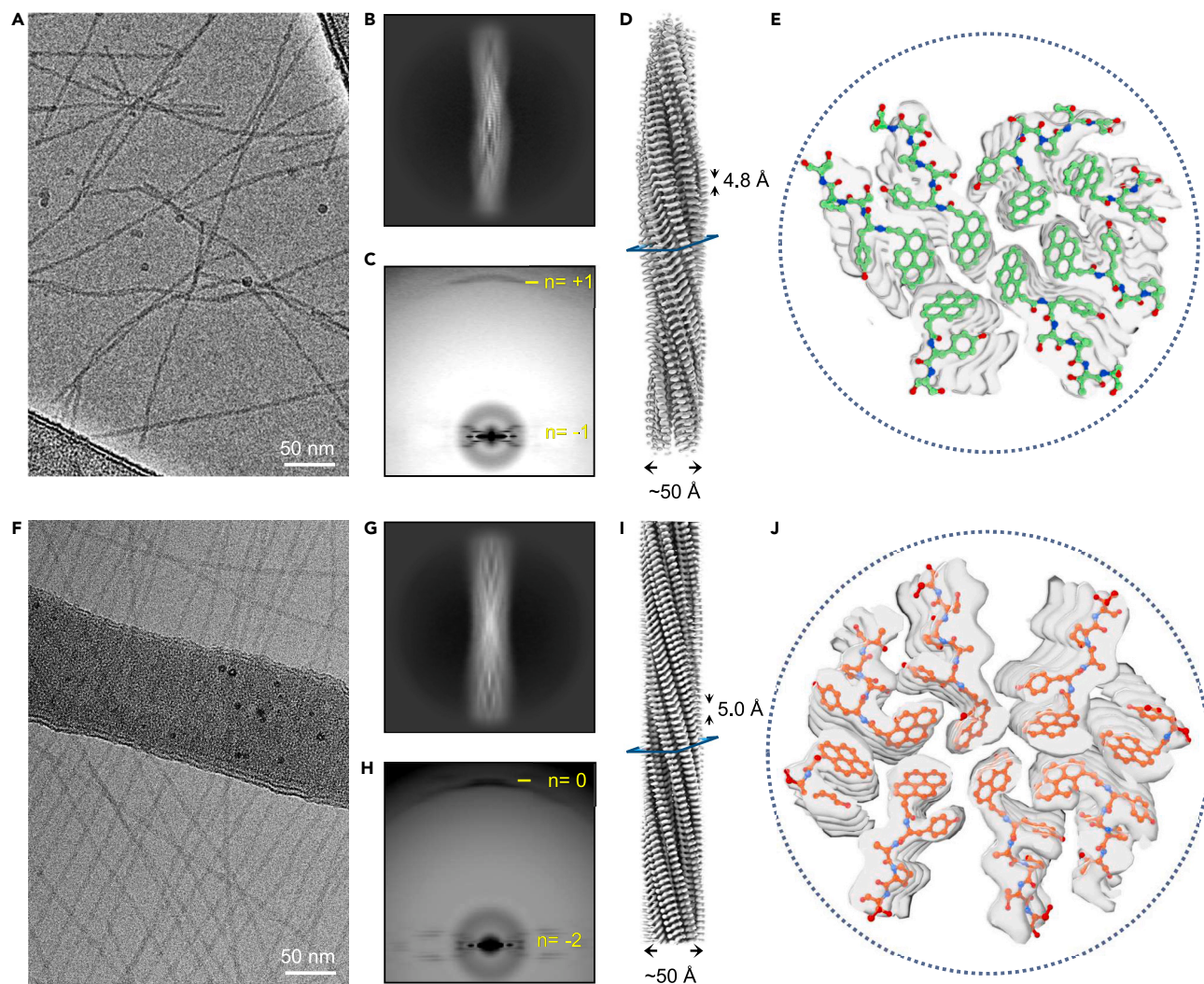


Figure 1. Cryo-EM structural reconstruction of the nanofibers of 1

(A) Representative cryo-EM image of the filaments of **1** (made at 1.3 mM, pH = 2). Lacey carbon grids were used for imaging.

(B and C) (B) 2D average, and (C) average power spectrum of nanofibers of **1** at pH = 2.

(D and E) (D) 3D helical reconstruction, and (E) the cross-section view of the nanofibers of **1** pH = 2.

(F) Representative cryo-EM image of the filaments of **1** (made at 1.3 mM, pH = 4.0, 2.0 mM Ca^{2+}). Lacey carbon grids were used for imaging.

(G and H) (G) 2D average, and (H) average power spectrum of nanofibers of **1** at pH = 4.0, 2.0 mM Ca^{2+} .

(I and J) (I) 3D helical reconstruction, and (J) the cross-section view of the nanofibers of **1** at pH = 4.0, 2.0 mM Ca^{2+} .

symmetry. The existence of a mirror plane in a 2D average is often used to judge the presence of an even number point group symmetry (e.g., C_2). Here, the average of the nanofiber at pH 2 without Ca^{2+} does not contain a mirror plane (Figure 1B), whereas the average of the nanofiber at pH 4 with Ca^{2+} does (Figure 1G). This result, together with well-separated cross- β densities (Figures 1D and 1I) and well-resolved peptide side chains (Figures 1E and 1J) in both nanofibers, validate the helical symmetry assignments.

We then asked what similarities and differences were present between the two nanofibers. Comparing the pyrene cores of both nanofibers reveals a conserved but slightly altered packing feature consisting of four pyrene rings (Figure 2A). This slight packing difference in the nanofiber with 2.0 mM Ca^{2+} allows one more pyrene ring to

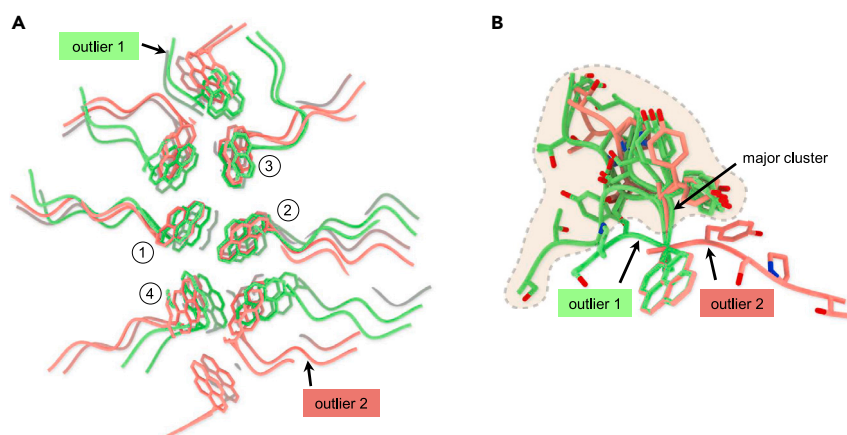


Figure 2. Slightly different architectures of nanofibers 1 under different conditions

(A) The alignment of two nanofiber structures reveals a conserved four pyrene packing. Green, the nanofiber 1 at pH 2; red, the nanofiber 1 at pH 4 with 2.0 mM Ca^{2+} . The well-aligned four pyrene rings are labeled.

(B) All unique peptides were aligned together by the pyrene ring. A major cluster of pyrene-tyrosine conformation was observed. Two outliers were highlighted in both (A) and (B).

stack during nanofiber formation. We think this is another example of quasi-equivalence, a concept originally introduced in icosahedral viruses in the 1960s⁴³ and recently discussed in helical assemblies⁴⁴: the existing plasticity in local pyrene contacts allows the nanofiber to adopt a slightly different helical symmetry. We next asked how many peptide conformations exist in those two nanofibers. Theoretically, there are seven unique environments in the nanofiber without Ca^{2+} and four in the nanofiber with Ca^{2+} (Figure S2). Alignment of all peptides by the pyrene rings shows a preferred cluster with respect to tyrosine and pyrene orientation. Two outliers were observed, but neither of those peptides packs in the conserved core of four pyrenes (Figure 2B).

Metal ions-induced self-assembly and nanofiber bundling

The structure of 1 suggests that calcium ions may promote self-assembly by interacting with the surface-exposed phosphate group of S7.⁴⁵ Bearing a pyrene motif, 1 tends to form excimers in an aqueous environment, displaying an ensemble of the monomer peaks (375–410 nm) and an excimer peak (~ 480 nm) in its fluorescence emission spectra of pyrene. The ratio of the excimer peak to the monomer peak offers a convenient assay for monitoring self-assembly. We first examined the Ca^{2+} responsiveness of 1 by observing changes in the fluorescence spectra. On the addition of Ca^{2+} , the intensity of the excimer peak increased, whereas that of the monomer peaks decreased (Figure 3A), indicating that Ca^{2+} promotes the self-assembly of 1. To quantify the monomeric and assembled portions of the phosphopeptapeptides on the addition of Ca^{2+} , we conducted peak deconvolution (Figure S3) and used the accumulative peak area of the excimer (A_e) and the monomer (A_m) to calculate the ratio of excimer to monomer (A_e/A_m). The A_e/A_m value increases gradually with the addition of Ca^{2+} from 0 to 2.0 mM, followed by a decrease after increasing the Ca^{2+} concentration from 2.2 to 2.8 mM (Figure 3B). The formation of aggregated 1 on the addition of 2.8 mM Ca^{2+} demonstrates reduced solubility of the growing assemblies, which led to a decline of A_e/A_m . The aggregate exhibited less fluorescence than the soluble 1 (Figure S4) due to aggregation-induced fluorescent quenching. To investigate how the interactions between 1 and Ca^{2+} change the secondary structure of 1, we monitored the change of the CD signal of 1 in the presence

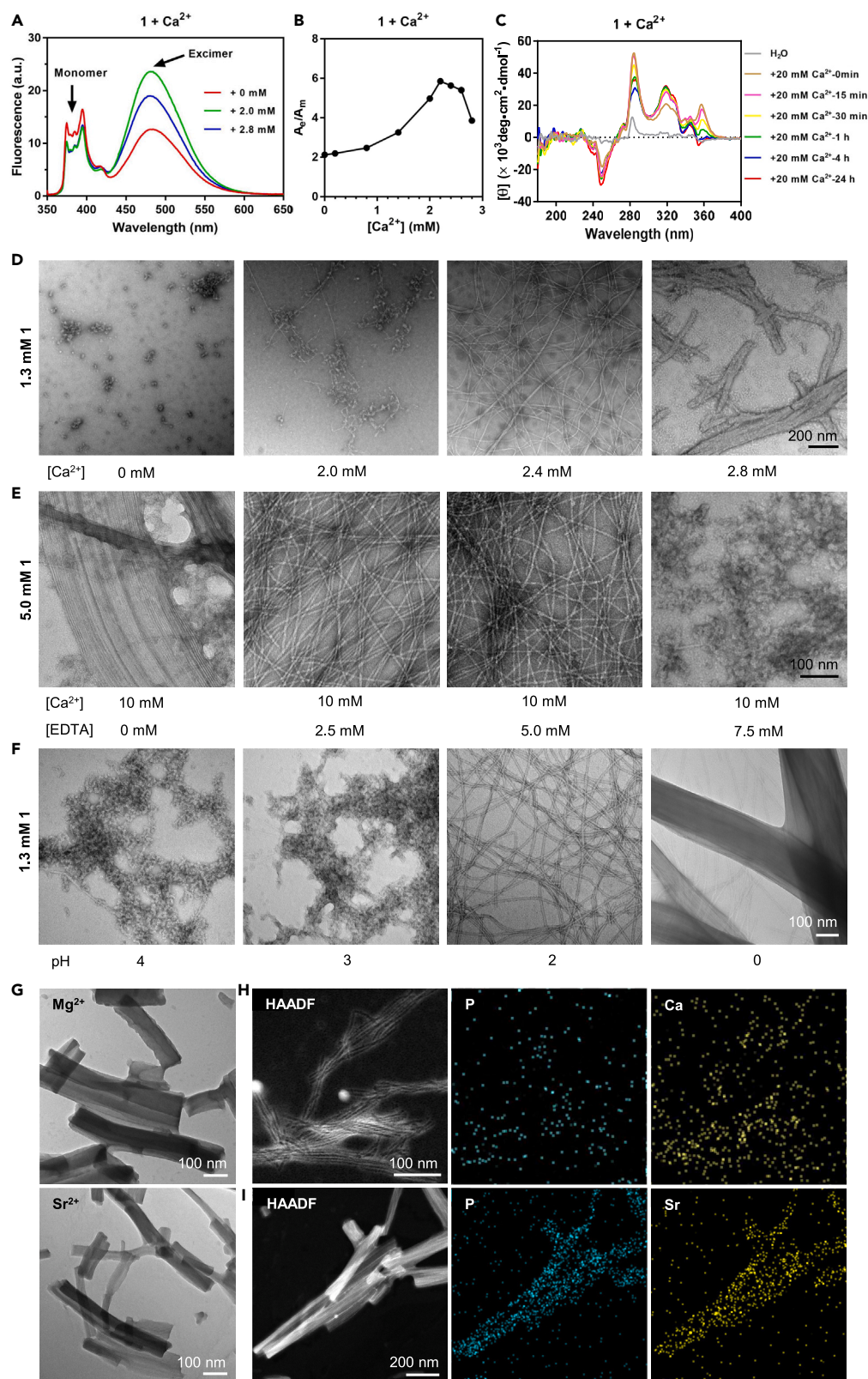


Figure 3. Metal-ion induced self-assembly of 1

(A) Fluorescence emission spectra of the effect of metal ions (1.3 mM) upon the addition of Ca^{2+} at different concentrations.
 (B) Pyrene excimer and monomer ratios (A_e/A_m) of 1 (1.3 mM) upon adding Ca^{2+} .
 (C) Circular dichroism spectra of 1 (1.3 mM) before and after Ca^{2+} (20 mM) addition and monitored at designated time points.
 (D) TEM images of 1 (1.3 mM) with different concentrations of Ca^{2+} (0–2.8 mM) for 3 h.
 (E) TEM images of 1 (5.0 mM) with Ca^{2+} (10 mM) on the addition of EDTA at different concentrations (0–7.5 mM) for 3 h.
 (F) TEM images of 1 (1.3 mM) at various pHs.
 (G) TEM images of 1 (1.3 mM) with Mg^{2+} (10 mM) or Sr^{2+} (10 mM) addition.
 (H and I) HAADF image and EDS mapping of (H) 1 (1.3 mM) + Ca^{2+} (2.8 mM) or (I) 1 (1.3 mM) + Sr^{2+} (10 mM). Samples were prepared in H_2O and incubated for 24 h unless indicated otherwise.

of Ca^{2+} over 24 h (Figures 3C and S5). The addition of calcium immediately changes the induced CD (ICD) signal (250–400 nm) from pyrene, whereas longer incubation gradually changes peak intensities (Figure 3C). The ICD changes agree with the increased bundle widths over time (vide infra) (Figure S6B).

We then sought to investigate the morphological changes of 1 on Ca^{2+} addition. As shown by TEM imaging, incubating 1 with different concentrations of Ca^{2+} transforms the nanoparticles into thin nanofibers. These nanofibers grow and entangle to form networks. Additionally, with the introduction of more Ca^{2+} , the interfibrillar interactions become stronger, resulting in the formation of filament bundles (Figure 3D). We also took TEM images of 1 + Ca^{2+} at increasing incubation time intervals to verify the process of hierarchical self-assembly. The results (Figure S6A) indicate that Ca^{2+} rapidly induces the formation of nanofibers and inter-filament interactions (magenta arrows). The nanofibers further group together and form bundles after 30 min (blue arrows). Subsequently, these nano-bundles continue to merge after 4 h, either into wider bundles (green arrows) or to form crossovers initiating the formation of bundles with a larger twist (yellow arrows). After 24 h of incubation, twisted bundles were observed (red arrow). The hierarchical self-assembly of 1 is supported by the increasing bundle width over time (Figure S6B). However, incubation of 1 (1.3 mM) in H_2O alone retains nanoparticle morphology (Figure S7). We speculate that this is because surface serine phosphates alone without Ca^{2+} are repulsive. Moreover, these noncovalent interactions facilitate interfibrillar stacking to generate self-oriented filaments and bundles. To determine the critical excimer formation concentration of 1 in the presence or absence of Ca^{2+} , we obtained the fluorescence emission spectra of 1 (0.020–1.3 mM) with or without Ca^{2+} (10 mM) (Figures S8A and S8B). The results of peak deconvolution and A_e/A_m values show significant excimer formation above 0.31 mM of 1 and that Ca^{2+} also further promotes the formation of excimers above the critical excimer concentration of 1 (Figures S8C, S9, and S10). We decreased the concentrations of 1 to 0.31, 0.16, and 0.080 mM, which led to fewer excimers (Figure S11A), and examined their responses to Ca^{2+} . At these concentrations, 1 only forms broken fibers or larger nanoparticles on Ca^{2+} addition (Figure S11B). These results confirm that the initial aggregation (excimer formation) of 1 is indispensable in filament bundle formation.

We also determined how the addition of Ca^{2+} transforms the morphology of 1 at various excimer-rich concentrations (0.63, 2.5, and 5.0 mM) (Figure S12A). As revealed by TEM, at 0.63, 2.5, and 5.0 mM in water and the addition of 2.8 mM of Ca^{2+} , 1 forms short bundles of nanofibers, separated nanofibers, and a mixture of nanoparticles and nanofibers, respectively (Figure S12B). This result indicates that the ratio between 1 and Ca^{2+} plays a key role in forming the assemblies. In addition to solubilizing 1 in water, we dissolved 1 in several biocompatible buffers, including PBS and Tris-HCl. TEM shows the formation of nanofibers and filament bundles on

the addition of Ca^{2+} to PBS or Tris-HCl-buffered solutions of **1**, respectively (Figures S13A and S13B). However, higher concentrations of Ca^{2+} are required for fiber formation. The hierarchical self-assembly of **1** incubated with Ca^{2+} is less sensitive to the buffer concentrations, evidenced by the bundle formation in Tris-HCl from 10 mM to 1 M (Figure S13C). Adding monovalent metal ions, such as Na^+ and K^+ (10 mM) into the solution of **1** (1.3 mM) results in the mixture containing nanofibers and amorphous particles (Figure S14A). In addition, we calculated the ionic strength, maintained the same ionic strength, and used TEM to examine the interaction of Ca^{2+} and Na^+ with **1**. At the same ionic strength, Ca^{2+} and Na^+ induce **1** to form bundles and nanofibers, respectively (Figure S14B). To determine whether the effects of salts on initial peptide solubility would affect the self-assembly of **1** with Ca^{2+} , we decreased the solubility of **1** by adding NaCl (100 mM) and incubated with or without calcium to investigate the changes in morphology. These results show that unlike calcium, although Na^+ induces nanofiber formation, it fails to initiate the hierarchical self-assembly of **1** to form bundles (Figure S15). These results confirm that the interactions between the phosphate group of **1** and Ca^{2+} are unique and specific. To exclude the possibility of negative staining-induced nanostructures, we determined the morphology of **1** incubated with Ca^{2+} , but without uranyl acetate (UA) staining (Figure S16). Although giving lower contrast than that with the UA staining, the TEM image shows the long bundles of filaments. The addition of ethylenediaminetetraacetic acid (EDTA), a calcium chelator, with increasing concentration, gradually dissociates the bundles made of **1** and Ca^{2+} to nanofibers and eventually to nanoparticles (Figure 3E). These results, thus, unambiguously confirm the interactions between **1** and Ca^{2+} for the formation of the filaments. Moreover, we found that at pH = 0, **1** also forms filament bundles (Figure 3F). Cryo-EM images of the bundles exclude the possibility of drying effects (Figure S17). Agreeing with the pKa of phosphate monoester ($\text{pK}_{\text{a}1} = 2.2$, $\text{pK}_{\text{a}2} = 5.8$),⁴⁶ the result indicates that reducing residual charges on the phosphate groups (or complete protonation of phosphates) of **1** promotes aggregation to form bundles and also suggests that decreasing pH produces similar effects compared with increasing calcium concentrations on filament formation of **1**.

Because the electrostatic interactions between the phosphates in **1** and calcium ions result in the filament bundles, other alkaline earth metal ions like Mg^{2+} or Sr^{2+} should lead to similar results. This assumption turns out to be valid. As shown by TEM (Figure 3G), adding Mg^{2+} or Sr^{2+} in the solution of **1** results in filament bundles, with **1** + Mg^{2+} generating larger assemblies than those of **1** + Sr^{2+} . These results indicate that the atomic sizes of the metal ions may also affect the nanostructures formed by **1**. This observation also suggests that electrostatic interactions contribute to filament formation. Similarly, **1** interacts with Mg^{2+} or Sr^{2+} to form filaments in the Tris-HCl buffer, with an increasing concentration of the metal ions to generate more rigid filaments (Figure S18).

To confirm the existence and to probe the distribution of the metal ions in the filaments, we conducted EDS mapping on the filaments formed by **1** with Ca^{2+} or Sr^{2+} (Figures 2H and 2I). The EDS mapping shows a correlated distribution of phosphorus with calcium or strontium. Notably, Sr^{2+} produces a better signal-to-noise ratio owing to its relatively high atomic number. The EDS mapping results also correspond with the EDS spectrum of a specific area in the nanostructures, where other elements such as C, O, N, and U are detected (Figure S19). Together with the HAADF-STEM and TEM images showing the filament bundles of **1** + Ca^{2+} (Figure S20), these results verify that the interactions between **1** and calcium ions result in bundle formation.

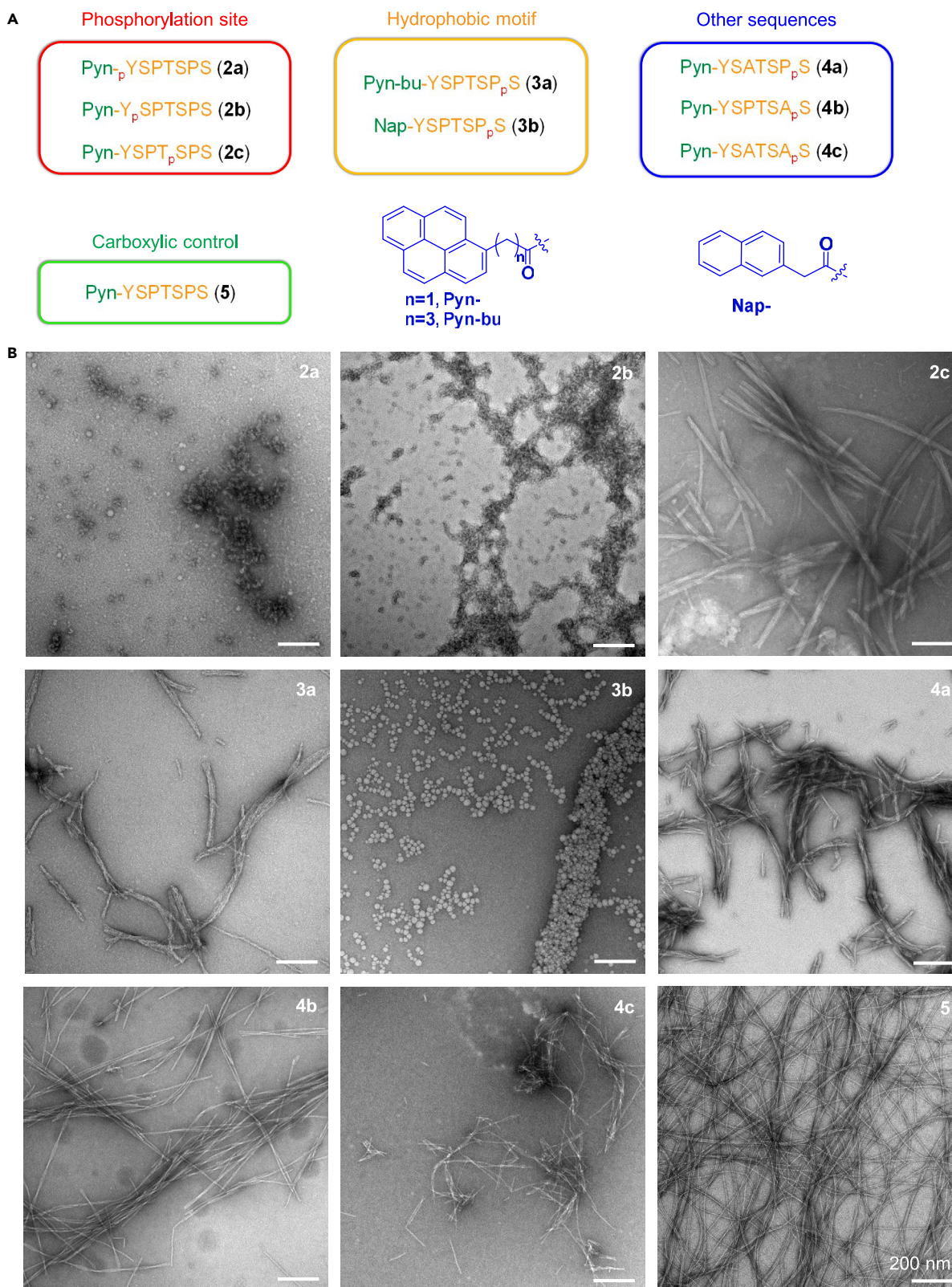


Figure 4. Self-assembly of the analogs of 1

(A) Molecular structures the analogs of 1 for determining the role of each structural motif in forming filaments via the calcium-enabled hierarchical assembly.

(B) TEM images of peptide analogs (1.3 mM) with Ca^{2+} (10 mM) addition in H_2O for 24 h.

Analogues of the IDP and their interactions with calcium ions

Although the single filaments have a global helical symmetry, the bundle is simply lacking global symmetry or any ordered repeating architecture for averaging. This is because filaments in the bundles do not necessarily pack in the register. In addition, some density regions of 1 were undetectable in the cryo-EM model (Figure S2). Thus, we designed nine analogs of 1 to further ascertain the factors contributing to single nanofiber and filament bundle formation. Specifically, we sought to investigate the significance of the (1) phosphorylation site position, (2) hydrophobic motif, (3) amino acid sequence, and (4) 1 without phosphorylation. Figure 4A shows the general design of the analogs, where LC-MS was used to confirm their identities (Figures S21–S32).

To validate whether phosphate accessibility is necessary from the nanofiber surface, we synthesized three analogs with phosphorylation at Tyr¹ (2a), Ser² (2b), and Ser⁵ (2c). As expected, deeply buried phosphorylation at Try¹ and Ser² (2a and 2b) produces amorphous aggregates and hardly results in filament formation, presumably due to the inaccessibility of the phosphorylation site for interacting with Ca^{2+} . Interestingly, the phosphorylation at Ser⁵, 2c, interacts with Ca^{2+} to produce filament bundles of smaller sizes (Figure 4B) when compared with those formed by 1. This result is consistent with the cryo-EM structure of 1, wherein Ser⁵ residues are observed to be solvent accessible in all peptide copies in the asymmetrical unit. These results suggest that the presence of phosphorylation near the nanofiber surface is crucial for Ca^{2+} -induced bundling.

To examine whether the pyrene core is essential for this type of nanofiber, we substituted the N-terminal hydrophobic pyrene in 1, with other hydrophobic groups (Figure 4A). Specifically, a pyrene derivative with a butyl spacer, Pyn-bu-, confers increased flexibility in the peptide's pyrene group (3a). In addition, a smaller aromatic residue, naphthyl (Nap), was also explored (3b). Interestingly, with the addition of Ca^{2+} , similar bundles with smaller diameters than 1 were observed for 3a, suggesting that the filament's core that was composed of the four fused benzene rings dominate the packing interactions and the short flexible linkers would be unlikely to significantly affect filament formation. When replacing the pyrene with the naphthyl motif (3b), filament formation is ultimately aborted, indicating that strong hydrophobic interactions (provided by pyrene in this study) are essential for the single filament architecture.

To understand the role of proline within the nanoparticles, we mutated one or both proline residues to alanine in 1 to generate three phosphopeptides (4a, 4b, and 4c). We were particularly interested in the structural contribution of proline residues because they are overrepresented in intrinsically disordered proteins.⁴⁷ TEM imaging analysis indicated that the loss of proline residues reduced the diameter of nanofiber bundles formed. Bundles of reduced width were seen in 4a and 4b, suggesting Pro⁶ adjacent to the phosphoserine aids the interaction between 1 and Ca^{2+} . Replacing both proline residues with alanines, 4c interacts with Ca^{2+} to form nanostructures similar to that of 4b + Ca^{2+} . Notably, mutating both proline residues to alanines in 4c resulted in increased filament formation when solubilized in water compared with 4a, 4b, and 1, indicating that alanine facilitates ordered self-assembly in water (Figure S33). These results suggest the "proline-phosphoserine" motif or sequence likely favors the morphology transformation that occurred on the addition of Ca^{2+} .

We synthesized **5** by removing the phosphate of the C-terminal serine. In this way, we examined the possibility of carboxylic acid interacting with alkaline earth metal ions to form bundles of filaments. After the addition of Ca^{2+} , Mg^{2+} , or Sr^{2+} to **5**, TEM images display individual nanofibers (Figures 4B and S34). These results confirm the crucial role of phosphoserine in the formation of nanofiber bundles. The above results suggest that the noncovalent, yet strong directional interactions and the presence and correct position of the proline-phosphoserine sequence in **1** are the two key contributors to the interactions between **1** and Ca^{2+} to form nanofiber bundles.

DISCUSSION

By obtaining the cryo-EM structure of the nanofibers of an IDP (**1**), this study provides the first structure of the supramolecular assemblies formed by intrinsically disordered short peptides. By examining the roles of phosphorylation, sequence, and noncovalent interactions, this work illustrates that the C-terminal proline-phosphoserine sequence and noncovalent interactions of the hydrophobic pyrenes are two crucial parameters in dictating the formation of the filament bundles in the presence of calcium ions. The hierarchical assembly of **1** in the presence of metal ions, together, with the structure of the nanofibers of **1** at near-atomic resolution, offers molecular insights into how the order arises from intrinsically disordered building blocks.

Although a considerable number of assemblies of pyrene-conjugated peptides have been reported,⁴⁸ structural detail is lacking. Contrasting to the previously suggested pyrene dimers in the assemblies, pyrenes form heptamers or octamers as the core of the peptide nanofibers. The arrangement of pyrene in the nanofibers formed by **1** represents a significant advancement of knowledge and will help understand other nanofiber assemblies formed by small molecules containing pyrene and peptides.^{49–52} Moreover, attaching large hydrophobic group (e.g., pyrene) to generate self-assembled nanofibers of an IDP for cryo-EM structural reconstruction may offer a general approach to reveal the most probable conformations of IDPs in the assemblies. Considering that fibrillar architectures are common in peptide assemblies, cryo-EM helical structural reconstruction is emerging as a powerful approach to obtain atomistic structures of other peptide assemblies that form helical polymers.^{14,53,54} In addition, the slightly different pyrene core packing observed under cryo-EM further emphasizes the cruciality of using cryo-EM structures as the starting point, but not as the end point of examination, for rational peptide design. An experimental model can provide more information, such as peptide-peptide interaction critical for filament formation, engineerable locations not contributing to the supramolecular structures, and structural plasticity of the assembly, etc., while the hypothetical model could be misleading and incomplete.^{42,55}

These results also underscore the combination of structural determination using cryo-EM single-particle reconstruction and chemistry is a powerful approach to understand hierarchical self-assembly processes involving IDPs. Cryo-EM maps of peptide assemblies at near-atomic resolution (better than 4.0 Å) offers a better alternative to small-angle X-ray scattering (SAXS) or nuclear magnetic resonance (NMR) for building a reliable atomic model.^{56,57} Moreover, this work explores the possibility of using metal ions in controlling interfibrillar interactions for generating higher-order assemblies, such as filament bundles. In addition, this work also implies the need to consider the role of calcium and magnesium ions, in addition to copper or zinc

ions,³⁸ in the pathology of other IDPs (e.g., β -amyloids) as calcium and magnesium ions mainly exist as metal ions at physiological conditions.

EXPERIMENTAL PROCEDURES

Resource availability

Lead contact

Further information and requests for resources should be directed to and will be fulfilled by the lead contact, Bing Xu (bxu@brandeis.edu).

Materials availability

The peptides reported in this work are available upon request.

Data and code availability

The supplementary figures generated during this study are available in the [supplemental information](#). The structural information generated in this study is available at the Protein Data Bank (PDB: 7UUQ and 8GI5).

Methods

Chemicals

2-Cl-trityl chloride resin (1.02 mmol/g), Fmoc protected amino acid building blocks, and 2-Naphthaleneacetic acid were purchased from GL Biochem (Shanghai, China). Fmoc-Osu was purchased from Creosalus. O-benzotriazole-N,N,N',N'-tetramethyluronium-hexafluorophosphate (HBTU) was purchased from Chem impex. N, N-diisopropylethylamine (DIPEA) and L-O-Phosphoserine were purchased from TCI America. 1-pyreneacetic acid and 1-pyrenebutyric acid were purchased from Sigma-Aldrich. Dimethylformamide (DMF), methylene chloride (DCM), trifluoroacetic acid (TFA), methanol (MeOH), triethylamine, and other reagents and solvents were purchased from Fisher Chemical. All reagents and solvents were used without further purification.

Instruments

All crude compounds were purified using a reverse phase HPLC (Agilent 1100 Series) with HPLC grade water (0.1% TFA) and HPLC grade acetonitrile (0.1% TFA) as eluents. LC-MS spectra were obtained on a Waters Acquity Ultra Performance Liquid Chromatography with Waters Micromass Quattro Mass Spectrometer. TEM was conducted on Morgagni 268 transmission electron microscope. HAADF-STEM and EDS were done on the FEI Titan Cubed Themis G2 300 TEM. CD was conducted on Jasco J-810 spectropolarimeter. Fluorescence emission spectra were obtained using Shimadzu RF-5301PC spectrometer. Cryo-EM was conducted on a Titan Krios (300 keV, Thermo Fisher) with a K3 camera (Gatan). pH was measured using Hydrion pH test paper (1.0–2.5; 3.0–5.5; 6.0–8.0; 9–13).

Peptide synthesis (1 as an example)

Compound 1 and its analogs were synthesized via solid-phase peptide synthesis (SPPS) using 2-chlorotrityl resin ([Scheme S1](#)). Resins were dipped in DCM for 15 min, and then the amino acid building blocks (2 mmol/g resin) in DMF were loaded using DIPEA to adjust pH to 8 for 1.5 h. Capping solution (DCM:MeOH:DIPEA = 17:2:1) was added for 20 min. 20% piperidine in DMF was added for 30 min for deprotection. For subsequent couplings, amino acids (2 mmol/g), HBTU (2 mmol/g), and DIPEA were loaded for 1 h. Wash with DMF after each step. Peptides were cleaved using a cleavage cocktail (95% TFA, 2.5% triisopropyl silane, and 2.5% H₂O) and reacted for 1 h. After concentration, ice-cold ethyl ether was added for peptide precipitation. The crude peptides were then purified by HPLC (purity > 97%).

Synthesis of O-phospho-L-tyrosine (p_Y)

Phosphorus pentoxide (10.0 g, 70.4 mmol) and 85% phosphoric acid (13.0 g) were added into a round-bottom flask under nitrogen gas protection. L-tyrosine (3.22 g, 17.8 mmol) was added when the system cools to 50°C–60°C. The reaction mixture was heated to 80°C and stirred for 24 h, with water (30 mL) added and stirred for 30 min to quench the reaction. The reaction mixture was cooled to room temperature and then added dropwise into cold n-butanol (650 mL). Collect the white precipitate through vacuum filtration and wash with ice water, ethanol, and ethyl ether. The white powder was lyophilized and used for the next step.

O-phospho-D-serine can be synthesized using this protocol.

Synthesis of Fmoc- p_Y

p_Y (0.5 g, 1.9 mmol) and Fmoc-Osu (0.78 g, 2.3 mmol) were added into 5 mL water and 5 mL acetonitrile. Triethylamine was added dropwise to adjust pH to 8.5–9.0. The reaction was stirred for 1 h at room temperature. Remove acetonitrile and add ethyl acetate (50 mL) and water (50 mL). Use 12 N hydrochloric acid to adjust pH to 2.0 and collect the organic phase. Furthermore, extract with ethyl acetate (2 × 50 mL). The organic phase was washed with 1 N hydrochloric acid (2 × 40 mL), water (2 × 40 mL), and brine (2 × 40 mL). Remove the solvents and collect the product. Purity: 99%.

Fmoc-(L)- p_S can also be synthesized using this protocol. Purity: 98%.

CD

CD spectra were recorded (180–400 nm) using a JASCO 8-10 spectrometer under nitrogen atmosphere. Peptide 1 was added into a quartz cuvette (1 mm) and scanned with 1 nm interval at the scanning speed of 100 nm/min for 3 times.

TEM

Glow discharge 400 mesh copper grids coated with carbon film and add 3 μ L sample. Let it stand for 1 min and then wash with 40 μ L ddH₂O. Stain the sample with 2% UA for 20 s, and air dry the grid. The grids were then imaged at a high tension of 80 kV.

HADDF-STEM

High-resolution HADDF-STEM images were obtained by using the Titan TEM equipped with a spherical aberration corrector, at an acceleration voltage of 300 kV.

Sample preparation

Peptides were dissolved in double-distilled water at 10 mM as stock solution. CaCl₂, MgCl₂, SrCl₂, NaCl, and KCl were dissolved in double-distilled water at 200 mM as stock solution. Samples that involve the addition of metal ions were directly diluted from the stock solution using double-distilled water or buffers (10, 20, 50 mM, or 1 M Tris-HCl [pH = 7.5]; PBS [pH = 7.4]). Samples that involve the addition of protons were directly diluted from peptide stock solution using double-distilled water and use 2 M hydrochloric acid to adjust pH to the desired value (Figures 1A, 1F, and 3F). All the samples are prepared and incubated at room temperature before characterization.

The pHs of samples in double-distilled water: 1.3 mM 1 in H₂O, pH = 4.0; 1.3 mM 1 + 2.0–20 mM Ca²⁺ in H₂O, pH = 4.0; 5.0 mM 1 + 2.8 mM Ca²⁺ in H₂O, pH = 3.0; 5.0 mM 1 + 10 mM Ca²⁺ in H₂O, pH = 3.0; 5.0 mM 1 + 10 mM Ca²⁺ + 2.5 mM EDTA in H₂O,

pH = 3.5; 5.0 mM **1** + 10 mM Ca^{2+} + 5.0 mM EDTA in H_2O , pH = 4.0; 5.0 mM **1** + 10 mM Ca^{2+} + 7.5 mM EDTA in H_2O , pH = 4.0; 2.5 mM **1** + 2.8 mM Ca^{2+} in H_2O , pH = 4.0; 0.63 mM **1** + 2.8 mM Ca^{2+} in H_2O , pH = 4.5; 0.31 mM **1** + 2.8 mM Ca^{2+} in H_2O , pH = 4.5; 0.16 mM **1** + 2.8 mM Ca^{2+} in H_2O , pH = 5.0; 0.080 mM **1** + 2.8 mM Ca^{2+} in H_2O , pH = 5.0; 1.3 mM **1** + 10 mM K^+ in H_2O , pH = 4.0; 1.3 mM **1** + 10 mM Na^+ in H_2O , pH = 4.0; 1.3 mM **1** + 30 mM Na^+ in H_2O , pH = 4.0; 1.3 mM **1** + 100 mM Na^+ in H_2O , pH = 4.0; 1.3 mM **1** + 100 mM Na^+ + 20 mM Ca^{2+} in H_2O , pH = 4.0; 1.3 mM **1** + 10 mM Mg^{2+} in H_2O , pH = 4.0; 1.3 mM **1** + 10 mM Sr^{2+} in H_2O , pH = 4.0; 1.3 mM analogs of **1** in H_2O , pH = 4.0; 1.3 mM analogs of **1** + 10 mM Ca^{2+} in H_2O , pH = 4.0; 1.3 mM **5** + 10 mM Mg^{2+} in H_2O , pH = 4.0; and 1.3 mM **5** + 10 mM Sr^{2+} in H_2O , pH = 4.0.

The pHs of samples in buffers: 1.3 mM **1** in 10 mM Tris-HCl (pH = 7.5), pH = 5.0; 1.3 mM **1** + 20 mM Ca^{2+} in 10 mM Tris-HCl (pH = 7.5), pH = 4.5; 1.3 mM **1** in 20 mM Tris-HCl (pH = 7.5), pH = 6.8; 1.3 mM **1** + 20 mM Ca^{2+} in 20 mM Tris-HCl (pH = 7.5), pH = 6.0; 1.3 mM **1** in 50 mM Tris-HCl (pH = 7.5), pH = 7.4; 1.3 mM **1** + 2.8–20 mM Ca^{2+} in 50 mM Tris-HCl (pH = 7.5), pH = 7.4; 1.3 mM **1** in 1 M Tris-HCl (pH = 7.5), pH = 7.6; 1.3 mM **1** + 20 mM Ca^{2+} in 1 M Tris-HCl (pH = 7.5), pH = 7.6; 1.3 mM **1** + 10 mM Mg^{2+} in 50 mM Tris-HCl (pH = 7.5), pH = 7.4; 1.3 mM **1** + 10 mM Sr^{2+} in 50 mM Tris-HCl (pH = 7.5), pH = 7.4; 1.3 mM **1** in PBS (pH = 7.4), pH = 6.4; and 1.3 mM **1** + 2.8–5.0 mM Ca^{2+} in PBS (pH = 7.5), pH = 6.4.

Cryo-EM of nanofiber

The peptide (**1**) samples (first sample at 1.3 mM, pH = 2, and second sample at 1.3 mM, pH = 4 and 2.0 mM Ca^{2+}) were applied to glow-discharged lacey carbon grids and vitrified using a Leica plunge freezer. Grids were imaged on a Titan Krios (300 keV, Thermo Fisher) with a K3 camera (Gatan). For the first sample, 6,233 micrographs were collected under electron counting mode at 1.08 Å per pixel, using a defocus range of 1–2 μm with ~ 50 electrons/Å² distributed into 40 fractions. For the second sample, 10,517 micrographs were collected under electron counting mode at 1.11 Å per pixel, using a defocus range of 1–2 μm with ~ 50 electrons/Å² distributed into 40 fractions. Motion correction and contrast transfer function (CTF) estimation were done in cryoSPARC.^{58–60} In both samples, a few million particles were auto picked by “Filament Tracer” with a shift of 15 or 18 pixels. Next, non-peptide junk particles and particles in low-resolution averages were removed by multiple rounds of reference-free 2D classifications. Particles having clear 2D average patterns were then selected. All possible helical symmetries were calculated from an averaged power spectrum of the raw particles and then were tested by trial and error in cryoSPARC until recognized peptide features, such as clear separation of β sheets and good side chains densities, were observed.^{29,61} The final volumes were then sharpened using local sharpening or DeepEMhancer available in cryoSPARC. Statistics are listed in Table S1.

Model building of filament

The (**1**) filament reached the $\sim 3.1/3.0$ Å resolution, respectively, according to map: map FSC. Since the filaments are made of only β sheets, the hand of the cryo-EM map cannot be determined directly. This is unlike cryo-EM maps that contain an α -helix, in which the hand is obvious when the resolution is 4.5 Å or better.²⁹ In the published cross- β structures, the parallel β sheets typically have a left-handed twist. However, this observation may not be deducible to short peptides containing non-standard residues. Therefore, we did model building for both hands of the map. First, the model was manually adjusted in Coot⁶² and then real-space refined in PHENIX.⁶³ The model fits better in the left-handed 1-start map than the right-handed 1-start

map in both cases, with better real space correlation coefficient (RSCC) (0.85 vs. 0.82, 0.85 vs. 0.84, respectively) and better hydrogen bonds within β sheets. Therefore, we suggested both maps probably have a left-handed twist in 1-start or 2-start, respectively. The refinement statistics of both (1) nanofibers are shown in Table S1.

SUPPLEMENTAL INFORMATION

Supplemental information can be found online at <https://doi.org/10.1016/j.chempr.2023.04.023>.

ACKNOWLEDGMENTS

This work is partially supported by NIH CA142746 (B.X.), GM122510 (E.H.E.), GM138756 (F.W.), and NSF DMR-2011846 (B.X.). This research was, in part, supported by the National Cancer Institute's National Cryo-EM Facility at the Frederick National Laboratory for Cancer Research under contract 75N91019D00024. The cryo-EM imaging was, in part, done at the Molecular Electron Microscopy Core Facility at the University of Virginia. The cryo-EM screening process was, in part, supported by the O'Neal Comprehensive Cancer Center at the University of Alabama Birmingham.

AUTHOR CONTRIBUTIONS

B.X. and J.G. conceived the study. J.G., under the supervision of B.X., designed and performed chemical synthesis, generated images of characterization, and analyzed the results. C.L. under the supervision of X.Z. performed STEM. Y.H. and M.Y. assisted in chemical synthesis. H.H. and W.T. performed LC-MS analysis. S.T.R.-N. and F.W. performed cryo-EM reconstructions and model building. J.G., S.T.R., E.H.E., F.W., and B.X. wrote the manuscript with input from all authors.

DECLARATION OF INTERESTS

The authors declare no competing interests.

Received: November 30, 2022

Revised: March 25, 2023

Accepted: April 27, 2023

Published: May 16, 2023

REFERENCES

- van der Lee, R., Buljan, M., Lang, B., Weatheritt, R.J., Daughdrill, G.W., Dunker, A.K., Fuxreiter, M., Gough, J., Gsponer, J., Jones, D.T., et al. (2014). Classification of intrinsically disordered regions and proteins. *Chem. Rev.* 114, 6589–6631. <https://doi.org/10.1021/cr40052>.
- Kumar, P., Paterson, N.G., Clayden, J., and Woolfson, D.N. (2022). De novo design of discrete, stable 310-helix peptide assemblies. *Nature* 607, 387–392. <https://doi.org/10.1038/s41586-022-04868-x>.
- Magnotti, E.L., Hughes, S.A., Dillard, R.S., Wang, S., Hough, L., Karumbamkandathil, A., Lian, T., Wall, J.S., Zuo, X., Wright, E.R., and Conticello, V.P. (2016). Self-assembly of an alpha-helical peptide into a crystalline two-dimensional nanoporous framework. *J. Am. Chem. Soc.* 138, 16274–16282. <https://doi.org/10.1021/jacs.6b06592>.
- Schneider, J.P., Pochan, D.J., Ozbas, B., Rajagopal, K., Pakstis, L., and Kretsinger, J. (2002). Responsive hydrogels from the intramolecular folding and self-assembly of a designed peptide. *J. Am. Chem. Soc.* 124, 15030–15037. <https://doi.org/10.1021/ja027993g>.
- Korevaar, P.A., Newcomb, C.J., Meijer, E.W., and Stupp, S.I. (2014). Pathway selection in peptide amphiphile assembly. *J. Am. Chem. Soc.* 136, 8540–8543. <https://doi.org/10.1021/ja503882s>.
- Hu, Y., Lin, R., Zhang, P., Fern, J., Cheetham, A.G., Patel, K., Schulman, R., Kan, C., and Cui, H. (2016). Electrostatic-driven lamination and untwisting of beta-sheet assemblies. *ACS Nano* 10, 880–888. <https://doi.org/10.1021/acsnano.5b06011>.
- Liu, X., Li, M., Liu, J., Song, Y., Hu, B., Wu, C., Liu, A.A., Zhou, H., Long, J., Shi, L., et al. (2022). In situ self-sorting peptide assemblies in living cells for simultaneous organelle targeting. *J. Am. Chem. Soc.* 144, 9312–9323. <https://doi.org/10.1021/jacs.2c01025>.
- Garcia, A.M., Iglesias, D., Parisi, E., Styan, K.E., Waddington, L.J., Deganutti, C., De Zorzi, R., Grassi, M., Melchionna, M., Vargiu, A.V., and Marchesan, S. (2018). Chirality effects on peptide self-assembly unraveled from molecules to materials. *Chem* 4, 1862–1876. <https://doi.org/10.1016/j.chempr.2018.05.016>.
- She, S., Bell, N.L., Zheng, D., Mathieson, J.S., Castro, M.D., Long, D.L., Koehnke, J., and Cronin, L. (2022). Robotic synthesis of peptides containing metal-oxide-based amino acids. *Chem* 8, 2734–2748. <https://doi.org/10.1016/j.chempr.2022.07.007>.
- Ji, W., Yuan, C., Chakraborty, P., Makam, P., Bera, S., Rencus-Lazar, S., Li, J., Yan, X., and Gazit, E. (2020). Coassembly-induced

transformation of dipeptide amyloid-like structures into stimuli-responsive supramolecular materials. *ACS Nano* 14, 7181–7190.

11. Cai, Y., Shen, H., Zhan, J., Lin, M., Dai, L., Ren, C., Shi, Y., Liu, J., Gao, J., and Yang, Z. (2017). Supramolecular “Trojan horse” for nuclear delivery of dual anticancer drugs. *J. Am. Chem. Soc.* 139, 2876–2879. <https://doi.org/10.1021/jacs.6b12322>.
12. Wang, C., Du, W., Wu, C., Dan, S., Sun, M., Zhang, T., Wang, B., Yuan, Y., and Liang, G. (2022). Cathepsin B-initiated Cypate nanoparticle formation for tumor photoacoustic imaging. *Angew. Chem. Int. Ed. Engl.* 61, e202114766. <https://doi.org/10.1002/anie.202114766>.
13. Wang, J., Hu, L., Zhang, H., Fang, Y., Wang, T., and Wang, H. (2022). Intracellular condensates of oligopeptide for targeting lysosome and addressing multiple drug resistance of cancer. *Adv. Mater.* 34, e2104704. <https://doi.org/10.1002/adma.202104704>.
14. He, H., Tan, W., Guo, J., Yi, M., Shy, A.N., and Xu, B. (2020). Enzymatic noncovalent synthesis. *Chem. Rev.* 120, 9994–10078. <https://doi.org/10.1021/acs.chemrev.0c00306>.
15. Álvarez, Z., Kolberg-Edelbrock, A.N., Sasselli, I.R., Ortega, J.A., Qiu, R., Sygiannis, Z., Mirau, P.A., Chen, F., Chin, S.M., Weigand, S., et al. (2021). Bioactive scaffolds with enhanced supramolecular motion promote recovery from spinal cord injury. *Science* 374, 848–856. <https://doi.org/10.1126/science.abh3602>.
16. Pires, R.A., Abul-Haija, Y.M., Costa, D.S., Novoa-Carballal, R., Reis, R.L., Ulijn, R.V., and Pashkuleva, I. (2015). Controlling cancer cell fate using localized biocatalytic self-assembly of an aromatic carbohydrate amphiphile. *J. Am. Chem. Soc.* 137, 576–579. <https://doi.org/10.1021/ja5111893>.
17. Tanaka, A., Fukuoka, Y., Morimoto, Y., Honjo, T., Koda, D., Goto, M., and Maruyama, T. (2015). Cancer cell death induced by the intracellular self-assembly of an enzyme-responsive supramolecular gelator. *J. Am. Chem. Soc.* 137, 770–775. <https://doi.org/10.1021/ja510156v>.
18. Jones, C.D., Kennedy, S.R., Walker, M., Yufit, D.S., and Steed, J.W. (2017). Scrolling of supramolecular lamellae in the hierarchical self-assembly of fibrous gels. *Chem* 3, 603–628. <https://doi.org/10.1016/j.chempr.2017.09.001>.
19. Feng, Z., Han, X., Wang, H., Tang, T., and Xu, B. (2019). Enzyme-instructed peptide assemblies selectively inhibit bone tumors. *Chem* 5, 2442–2449. <https://doi.org/10.1016/j.chempr.2019.06.020>.
20. He, H., Lin, X., Wu, D., Wang, J., Guo, J., Green, D.R., Zhang, H., and Xu, B. (2020). Enzymatic noncovalent synthesis for mitochondrial genetic engineering of cancer cells. *Cell Rep. Phys. Sci.* 1, 100270. <https://doi.org/10.1016/j.xcrp.2020.100270>.
21. Reches, M., and Gazit, E. (2003). Casting metal nanowires within discrete self-assembled peptide nanotubes. *Science* 300, 625–627. <https://doi.org/10.1126/science.1082387>.
22. Chen, Z., Chen, M., Zhou, K., and Rao, J. (2020). Pre-targeted imaging of protease activity through in situ assembly of nanoparticles. *Angew. Chem. Int. Ed. Engl.* 59, 7864–7870. <https://doi.org/10.1002/anie.201916352>.
23. Medina, S.H., Miller, S.E., Keim, A.I., Gorka, A.P., Schnermann, M.J., and Schneider, J.P. (2016). An intrinsically disordered peptide facilitates non-endosomal cell entry. *Angew. Chem.* 128, 3430–3433. <https://doi.org/10.1002/ange.201510518>.
24. Jacoby, G., Segal Asher, M., Ehm, T., Abutbul Ionita, I., Shinar, H., Azoulay-Ginsburg, S., Zemach, I., Koren, G., Danino, D., Kozlov, M.M., et al. (2021). Order from disorder with intrinsically disordered peptide amphiphiles. *J. Am. Chem. Soc.* 143, 11879–11888. <https://doi.org/10.1021/jacs.1c06133>.
25. Yang, D., He, H., Kim, B.J., and Xu, B. (2021). Peptide assemblies mimicking chaperones for protein trafficking. *Bioconj. Chem.* 32, 502–506. <https://doi.org/10.1021/acs.bioconjchem.1c00032>.
26. Li, J., Zhan, Z., Du, X., Wang, J., Hong, B., and Xu, B. (2018). Selection of secondary structures of heterotypic supramolecular peptide assemblies by an enzymatic reaction. *Angew. Chem. Int. Ed. Engl.* 57, 11716–11721. <https://doi.org/10.1002/anie.201806992>.
27. Yang, Y., Arseni, D., Zhang, W., Huang, M., Lövestam, S., Schweighauser, M., Kotecha, A., Murzin, A.G., Peak-Chew, S.Y., Macdonald, J., et al. (2022). Cryo-EM structures of amyloid-beta 42 filaments from human brains. *Science* 375, 167–172. <https://doi.org/10.1126/science.abm7285>.
28. Portz, B., Lu, F., Gibbs, E.B., Mayfield, J.E., Rachel Mehaffey, M., Zhang, Y.J., Brodbelt, J.S., Showalter, S.A., and Gilmour, D.S. (2017). Structural heterogeneity in the intrinsically disordered RNA polymerase II C-terminal domain. *Nat. Commun.* 8, 15231. <https://doi.org/10.1038/ncomms15231>.
29. Wang, F., Gnewou, O., Solemanifar, A., Conticello, V.P., and Egelman, E.H. (2022). Cryo-EM of helical polymers. *Chem. Rev.* 122, 14055–14065. <https://doi.org/10.1021/acs.chemrev.1c00753>.
30. Kim, M., Krogan, N.J., Vasiljeva, L., Rando, O.J., Nedeia, E., Greenblatt, J.F., and Buratowski, S. (2004). The yeast Rat1 exonuclease promotes transcription termination by RNA polymerase II. *Nature* 432, 517–522. <https://doi.org/10.1038/nature03041>.
31. Mészáros, B., Tompa, P., Simon, I., and Dosztányi, Z. (2007). Molecular principles of the interactions of disordered proteins. *J. Mol. Biol.* 372, 549–561. <https://doi.org/10.1016/j.jmb.2007.07.004>.
32. Burley, S.K., and Petsko, G.A. (1985). Aromatic-aromatic interaction – a mechanism of protein-structure stabilization. *Science* 229, 23–28.
33. Narasumani, M., and Harrison, P.M. (2018). Discerning evolutionary trends in post-translational modification and the effect of intrinsic disorder: analysis of methylation, acetylation and ubiquitination sites in human proteins. *PLoS Comput. Biol.* 14, e1006349. <https://doi.org/10.1371/journal.pcbi.1006349>.
34. Uversky, V.N. (2013). Intrinsic disorder-based protein interactions and their modulators. *Curr. Pharm. Des.* 19, 4191–4213. <https://doi.org/10.2174/1381612811319230005>.
35. Xie, H., Vucetic, S., Iakoucheva, L.M., Oldfield, C.J., Dunker, A.K., Uversky, V.N., and Obradovic, Z. (2007). Functional anthology of intrinsic disorder. 1. Biological processes and functions of proteins with long disordered regions. *J. Proteome Res.* 6, 1882–1898. <https://doi.org/10.1021/pr060392u>.
36. Ardito, F., Giuliani, M., Perrone, D., Troiano, G., and Lo Muzio, L. (2017). The crucial role of protein phosphorylation in cell signaling and its use as targeted therapy (Review). *Int. J. Mol. Med.* 40, 271–280. <https://doi.org/10.3892/ijmm.2017.3036>.
37. Breydo, L., and Uversky, V.N. (2011). Role of metal ions in aggregation of intrinsically disordered proteins in neurodegenerative diseases. *Metallomics* 3, 1163–1180. <https://doi.org/10.1039/c1mt00106j>.
38. Faller, P., Hureau, C., and La Penna, G. (2014). Metal ions and intrinsically disordered proteins and peptides: from Cu/Zn amyloid-beta to general principles. *Acc. Chem. Res.* 47, 2252–2259. <https://doi.org/10.1021/ar400293h>.
39. Kollmer, M., Close, W., Funk, L., Rasmussen, J., Bsoul, A., Schierhorn, A., Schmidt, M., Sigurdson, C.J., Jucker, M., and Fändrich, M. (2019). Cryo-EM structure and polymorphism of Abeta amyloid fibrils purified from Alzheimer's brain tissue. *Cell. Commun.* 10, 4760. <https://doi.org/10.1038/s41467-019-12683-8>.
40. Yang, Y., Shi, Y., Schweighauser, M., Zhang, X., Kotecha, A., Murzin, A.G., Garringer, H.J., Cullinane, P.W., Saito, Y., Foroud, T., et al. (2022). Structures of alpha-synuclein filaments from human brains with Lewy pathology. *Nature* 610, 791–795. <https://doi.org/10.1038/s41586-022-05319-3>.
41. Lövestam, S., Koh, F.A., van Knippenberg, B., Kotecha, A., Murzin, A.G., Goedert, M., and Scheres, S.H.W. (2022). Assembly of recombinant tau into filaments identical to those of Alzheimer's disease and chronic traumatic encephalopathy. *eLife* 11, e76494. <https://doi.org/10.7554/eLife.76494>.
42. Wang, F., Gnewou, O., Wang, S., Osinski, T., Zuo, X., Egelman, E.H., and Conticello, V.P. (2021). Deterministic chaos in the self-assembly of β sheet nanotubes from an amphipathic oligopeptide. *Matter* 4, 3217–3231. <https://doi.org/10.1016/j.matt.2021.06.037>.
43. Caspar, D.L., and Klug, A. (1962). Physical principles in the construction of regular viruses. *Cold Spring Harb. Symp. Quant. Biol.* 27, 1–24. <https://doi.org/10.1101/sqb.1962.027.001.005>.
44. Wang, F., Cvirkaitė-Krupovic, V., Vos, M., Beltran, L.C., Kreutzberger, M.A.B., Winter, J.M., Su, Z., Liu, J., Schouten, S., Krupovic, M., et al. (2022). Spindle-shaped archaeal viruses evolved from rod-shaped ancestors to package a larger genome. *Cell* 185, 1297–1307.e11. <https://doi.org/10.1016/j.cell.2022.02.019>.
45. George, A., and Veis, A. (2008). Phosphorylated proteins and control over apatite nucleation, crystal growth, and inhibition. *Chem. Rev.* 108, 4670–4693. <https://doi.org/10.1021/cr0782729>.
46. Hunter, T. (2012). Why nature chose phosphate to modify proteins. *Philos. Trans. R. Soc. Lond.*

- B Biol. Sci. 367, 2513–2516. <https://doi.org/10.1098/rstb.2012.0013>.
47. Babu, M., Favretto, F., Rankovic, M., and Zweckstetter, M. (2022). Peptidyl prolyl isomerase A modulates the liquid-liquid phase separation of proline-rich IDPs. *J. Am. Chem. Soc.* 144, 16157–16163. <https://doi.org/10.1021/jacs.2c07149>.
48. Li, J., Du, X., Hashim, S., Shy, A., and Xu, B. (2017). Aromatic–aromatic interactions enable α -helix to β -sheet transition of peptides to form supramolecular hydrogels. *J. Am. Chem. Soc.* 139, 71–74. <https://doi.org/10.1021/jacs.6b11512>.
49. Xing, B., Yu, C.-W., Chow, K.-H., Ho, P.-L., Fu, D., and Xu, B. (2002). Hydrophobic interaction and hydrogen bonding cooperatively confer a vancomycin hydrogel: A potential candidate for biomaterials. *J. Am. Chem. Soc.* 124, 14846–14847. <https://doi.org/10.1021/ja028539f>.
50. Jeena, M.T., Palanikumar, L., Go, E.M., Kim, I., Kang, M.G., Lee, S., Park, S., Choi, H., Kim, C., Jin, S.M., et al. (2017). Mitochondria localization induced self-assembly of peptide amphiphiles for cellular dysfunction. *Nat. Commun.* 8, 26. <https://doi.org/10.1038/s41467-017-00047-z>.
51. Lin, Y.X., Qiao, S.L., Wang, Y., Zhang, R.X., An, H.W., Ma, Y., Rajapaksha, R.P., Qiao, Z.Y., Wang, L., and Wang, H. (2017). An in situ intracellular self-assembly strategy for quantitatively and temporally monitoring autophagy. *ACS Nano* 11, 1826–1839. <https://doi.org/10.1021/acs.nano.6b07843>.
52. Brea, R.J., Vázquez, M.E., Mosquera, M., Castedo, L., and Granja, J.R. (2007). Controlling multiple fluorescent signal output in cyclic peptide-based supramolecular systems. *J. Am. Chem. Soc.* 129, 1653–1657. <https://doi.org/10.1021/ja066885h>.
53. Miller, J.G., Hughes, S.A., Modlin, C., and Conticello, V.P. (2022). Structures of synthetic helical filaments and tubes based on peptide and peptido-mimetic polymers. *Q. Rev. Biophys.* 55, 1–103. <https://doi.org/10.1017/S0033583522000014>.
54. Kreutzberger, M.A.B., Wang, S., Beltran, L.C., Tuachi, A., Zuo, X., Egelman, E.H., and Conticello, V.P. (2022). Phenol-soluble modulins PSM α 3 and PSM β 2 form nanotubes that are cross- α amyloids. *Proc. Natl. Acad. Sci. USA* 119, e2121586119. <https://doi.org/10.1073/pnas.2121586119>.
55. Pieri, L., Wang, F., Arteni, A.A., Vos, M., Winter, J.M., Le Du, M.H., Artzner, F., Gobeaux, F., Legrand, P., Boulard, Y., et al. (2022). Atomic structure of lanreotide nanotubes revealed by cryo-EM. *Proc. Natl. Acad. Sci. USA* 119, e2120346119. <https://doi.org/10.1073/pnas.2120346119>.
56. Wang, R.Y., Kudryashev, M., Li, X., Egelman, E.H., Basler, M., Cheng, Y., Baker, D., and DiMaio, F. (2015). De novo protein structure determination from near-atomic-resolution cryo-EM maps. *Nat. Methods* 12, 335–338. <https://doi.org/10.1038/nmeth.3287>.
57. DiMaio, F., Yu, X., Rensen, E., Krupovic, M., Prangishvili, D., and Egelman, E.H. (2015). Virology. A virus that infects a hyperthermophile encapsidates A-form DNA. *Science* 348, 914–917. <https://doi.org/10.1126/science.aaa4181>.
58. Zheng, S.Q., Palovcak, E., Armache, J.P., Verba, K.A., Cheng, Y., and Agard, D.A. (2017). MotionCor2: anisotropic correction of beam-induced motion for improved cryo-electron microscopy. *Nat. Methods* 14, 331–332. <https://doi.org/10.1038/nmeth.4193>.
59. Rohou, A., and Grigorieff, N. (2015). CTFFIND4: fast and accurate defocus estimation from electron micrographs. *J. Struct. Biol.* 192, 216–221. <https://doi.org/10.1016/j.jsb.2015.08.008>.
60. Punjani, A., Rubinstein, J.L., Fleet, D.J., and Brubaker, M.A. (2017). cryoSPARC: algorithms for rapid unsupervised cryo-EM structure determination. *Nat. Methods* 14, 290–296. <https://doi.org/10.1038/nmeth.4169>.
61. Egelman, E.H. (2000). A robust algorithm for the reconstruction of helical filaments using single-particle methods. *Ultramicroscopy* 85, 225–234. [https://doi.org/10.1016/S0304-3991\(00\)00062-0](https://doi.org/10.1016/S0304-3991(00)00062-0).
62. Emsley, P., and Cowtan, K. (2004). Coot: model-building tools for molecular graphics. *Acta Crystallogr. D Biol. Crystallogr.* 60, 2126–2132. <https://doi.org/10.1107/S0907444904019158>.
63. Afonine, P.V., Poon, B.K., Read, R.J., Sobolev, O.V., Terwilliger, T.C., Urzhumtsev, A., and Adams, P.D. (2018). Real-space refinement in PHENIX for cryo-EM and crystallography. *Acta Crystallogr. D Struct. Biol.* 74, 531–544. <https://doi.org/10.1107/S2059798318006551>.